Applied Geochemistry 207 (2026) 106961

Contents lists available at ScienceDirect

Applied Geochemistry

journal homepage: www.elsevier.com/locate/apgeochem

Effects of secondary hydrothermal fluids on gallium distribution and coordination in hot springs silica using Ga K-edge XANES

M.C. Rowe [a,*], K.A. Campbell [a], D.A. Stallard [a], B. Lyon [a], A. Langendam [b], E. Kalinina [c], M. Yamanaka [c], R. Tanaka [c], T. Christopher [d], S.W. Ruff [e], E. Nersezova [a], T. Ota [c], A. Hamilton [a]

[a] *School of Environment, University of Auckland, Auckland, 1142, New Zealand*
[b] *Australian Synchrotron Facility (Ansto), Clayton, VIC, 3168, Australia*
[c] *The Pheasant Memorial Laboratory for Geochemistry and Cosmochemistry, Institute for Planetary Materials, Okayama University, Misasa, Tottori, 682-0193, Japan*
[d] *School of Chemical Sciences, University of Auckland, Auckland, 1142, New Zealand*
[e] *Arizona State University, School of Earth And Space Exploration, Tempe, AZ, 85287, USA*

ARTICLE INFO

Editorial handling by: Elisa Sacchi

Keywords:
Hot springs
New Zealand
Gallium
Sinter
Synchrotron radiation
Coordination number

ABSTRACT

Gallium (Ga), a critical element in the electronics industry, is enriched in hot spring silica deposits (sinter) at concentrations comparable to, and in some cases greater than, bauxite, coal, and sphalerite deposits from which it is currently extracted. Focusing on well characterized Holocene and Pleistocene New Zealand sinters, we utilize synchrotron-X-ray fluorescence (sXRF) and Ga K-edge X-ray absorption near edge structure (XANES) spectroscopy to examine the spatial distribution of Ga as well as its changing coordination number. Ga^{+3} is the only observed oxidation state in the analyzed sinters. Gallium is predominantly found in tetrahedral coordination in sinter deposited from alkali chloride fluids, with analyses best matching Ga-aluminosilicate standards. However, Ga coordination is octahedral in sinter samples that have undergone alteration by acidic fluids/gases, associated with a change in hydrology from alkali-chloride to acid-sulfate fluid conditions. High Ga concentrations are found associated with both these coordination environments, with a heterogeneous distribution. Octahedral Ga is observed both as particles and in larger regions affected by Fe-rich fluid overprinting. The combined use of sXRF and XANES demonstrates an ability to fingerprint diagenesis and alteration in these complex geothermal settings where tetrahedral and octahedral Ga co-exist. The transition from tetrahedral to octahedral Ga also appears to mimic the inferred natural process forming lateritic bauxite deposits, where remobilized tetrahedral Ga is reconcentrated and adsorbed to oxides. A similar process may occur for sinter Ga enrichment, whereby introduced Ga in acidic conditions is adsorbed to oxide phases as the Fe-rich secondary fluids infiltrate porous sinter material.

1. Introduction

Gallium (Ga) is a critical metal in electronic components utilizing GaAs and GaN in today's technology driven society (Moskalyk, 2003; Lu et al., 2017). While it is found in low abundances in many different materials (i.e. average Ga abundance in crustal materials is ∼16 to 17 ppm; Burton et al., 1959; Rudnick and Gao, 2003), Ga is a major chemical constituent in only four rare, naturally occurring minerals (Foley et al., 2017). At Earth's surface the most stable form of Ga found in nature is as a +3 cation (F. Li et al., 2022; Yuan et al., 2021). While there are limited conditions under which Ga may exist in more reduced forms, even those are debated (Ga^{+}; Frick et al., 2000; Yuan et al., 2021) and it is generally not considered to be redox active (Hagvall et al., 2014). As a result of its comparable ionic radius and charge, Ga^{3+} may substitute for Al^{3+} in many geologic materials, such as bauxite, the primary ore for Ga (Yuan et al., 2021), and it is a common constituent in aluminosilicate minerals, with higher concentrations in some feldspars and micas (e.g., Burton et al., 1959; Foley et al., 2017). In fact, the separation of Al from Ga in extraction processes is generally challenging because of the similarities in chemical properties between the two elements (e.g., Chen et al., 2025). The separation of Ga from Al is also a key step in recovering Ga from Bayer liquor – a hot concentrated solution of

---

* Corresponding author.
E-mail address: Michael.rowe@auckland.ac.nz (M.C. Rowe).

https://doi.org/10.1016/j.apgeochem.2026.106961
Received 26 March 2026; Received in revised form 20 June 2026; Accepted 25 June 2026

NaOH used in the industrial extraction of alumina from bauxite ore – which is the source for ~90% of the world's Ga supply (Zhao et al., 2012). Sphalerite and magnetite may also be enriched in Ga, where it substitutes for Fe (Foley et al., 2017) and, although the mechanisms are less clear, Ga is sequestered in organic materials such as coal (Goldschmidt, 1937; Qin et al., 2015). From its similar electronegativity, ionic radius and Me^{3+}–O bond distance (Frick et al., 2000), Ga is also proposed to be enriched by microbial processes through mimicry of Fe^{3+}, a critical nutrient for microbial survival (e.g., Minandri et al., 2014; Li, F. et al., 2022). Thus, there are multiple mechanisms for Ga enrichment, with bauxite, sphalerite, and coal deposits currently the three largest sources for Ga (Lu et al., 2017). However, the concentrations of Ga in these deposit types are quite low (on average < 100 ppm), such that Ga is only extracted as a by-product of other mining activity (e.g., Foley et al., 2017).

Geothermal fluids have long been recognized as potentially important sources for "high-value" metals (e.g., Li, Cs, Au, Ag; Krupp and Seward, 1987; Pope et al., 2005; Lo et al., 2014). Silica deposits formed from the precipitation of geothermal fluids are also often variably enriched in a wide range of metals of interest (e.g., Weissberg, 1969; Rice et al., 1995; Guido et al., 2002; Hamilton et al., 2017; Sanchez-Yanez et al., 2017). Gallium in hot spring sinter is relatively ubiquitous but is heterogeneously distributed, potentially sequestered by microbial processes (Gangidine et al., 2020) and controlled by silica polymerization (Lyon et al., 2026). Gallium concentrations (from 10's to 100's of ppm) in sinter are often comparable to other natural Ga resources (e.g. bauxite, coal, sphalerite; Lu et al., 2017; Foley et al., 2017; Havig et al., 2021). Moreover, Ga concentrations may reach up to 800 ppm (bulk analysis; Havig et al., 2021) or up to ~1500 ppm (in situ microanalysis; Nersezova et al., 2024), despite relatively low abundances in geothermal fluids (e.g., typically below 28 ppb, or 400 nM, in geothermal fluids at Yellowstone National Park, USA; Havig et al., 2021). Silica phase mineral maturation can significantly impact the distribution of metals, forcing trace chemical constituents out during recrystallization, which may result in the further concentration of these metals (Sanchez-Yanez et al., 2017). On the other hand, gallium, may be retained within the silica phase during recrystallization, with discrete textures evident even in Jurassic-aged sinter deposits, which are fully recrystallized to quartz (Nersezova et al., 2024). Within silica deposits, hydrothermal alteration and overprinting of primary sinter textures with secondary fluids can also significantly impact the distribution of Ga along with other trace metals. Lyon et al. (2026) highlight multiple compositionally distinct fluids variably enriched in Ga, which overprint primary textures associated with sinter formation (cf. Gangidine et al., 2020). In contrast, Rowe et al. (2025) highlight the redistribution of Fe, but the retention of Ga, from fumarolic alteration, resulting in not just a redistribution of elements but a chemical separation (i.e., fractionation) as well.

Chemical extraction processes of metals from rocks and minerals depend on their local atomic environment. Since Ga is found in compositionally distinct deposits, as noted above, extraction processes are also variable (Lu et al., 2017). Apart from its heterogeneous spatial distribution and variable concentrations (Gangidine et al., 2020; Nersezova et al., 2024; Rowe et al., 2025; Lyon et al., 2026), little is known about the chemical environment of Ga in solid sinter deposits. The solubility of gallium oxyhydroxide (α-GaOOH), relevant to bauxite deposits, is generally low, with a minimum at a pH of ~4, but increases at both low (<3) and high (>8) pH and with increasing temperature (Wood and Samson, 2006; Lu et al., 2017). However, Ga in bauxite deposits is thought to originally be enriched from the weathering of aluminosilicate minerals, resulting in the adsorption of Ga^{3+} to oxide minerals, and its potential subsequent replacement for Al^{3+} and Fe^{3+} (Qi et al., 2023), suggesting significant changes to the local chemical environment of Ga through natural geologic processing. Variability in Ga coordination number is observed with both $^{[4]}$Ga (tetrahedral [4]-coordination) and $^{[6]}$Ga (octahedral [6]-coordination) found in geologic materials under surface conditions, where $^{[X]}$Ga refers to [X] coordination number in Ga. In solids composed of oxygen anions, Ga^{3+} has a radius ratio that is near the transition between [4] and [6] coordination environments (Frick et al., 2000). For example, in feldspars, Ga is present in a [4]-coordination environment (Mare et al., 2021), yet it is found as both [4] and [6]-coordination in β-Ga_2O_3 (Nishi et al., 1998) and only in [6]-coordination in ZnGa-spinel (Mare et al., 2021). In addition, when considering possible organo-metal ligands, metal-organic bonds (as observed in metal-organic frameworks; MOFs) may have greater diversity in bond length and changes in coordination geometry resulting from the easily changed bond angles (Morris and Brammer, 2017). Thus, Ga has the potential to preserve variable coordination chemistry depending on changes to its local chemical environment, which may mirror the different geologic deposits in which it is associated with in nature (Foley et al., 2017; Lu et al., 2017).

To better understand the chemical environment of Ga in hot spring systems and whether it changes as a result of geologic processes, we investigate changes in Ga oxidation state and coordination geometry in sinter utilizing X-ray absorption near edge structure (XANES) spectroscopy. XANES spectroscopy is integrated with petrologic analysis and elemental concentrations to provide a broader understanding of Ga coordination, important for chemical extraction, in a complex geologic setting where, despite chemical and spatial variability, Ga concentrations (cf. Havig et al., 2021) are comparable to other key Ga resources (Foley et al., 2017).

2. Materials and methods

2.1. Samples

This study investigates 11 Late Pleistocene (defined here as the interval from about 129 000 to 11 700 years ago) to Holocene age (i.e., younger than ~11 700 years ago), siliceous hot spring (i.e. sinter) samples from across the Taupō Volcanic Zone (TVZ), New Zealand, including Orakei Korako, Ohakuri, Whangapaoa Spring, Te Kopia, Waiotapu, and Wairakei, derived from a 20+ year sinter collection at the University of Auckland (Table 1). For comparison to the sinter samples, an additional sample of hydrothermal colloform-textured opaline silica, overlying highly brecciated sinter, from the Opal Mound region at Roosevelt Hot Springs geothermal site located in Utah, U.S.A. (Parry et al., 1977; Lynne et al., 2005) is included as an inferred high temperature end-member.

Sinter samples used in this study represent distinct lithofacies (sensu Cady and Farmer, 1996), derived from alkali chloride hot springs of high-temperature (~70-100 °C) spring-vent areas, through mid-temperature (~45-65 °C) mid-apron discharge channels and pools, to low-temperature (~25-40 °C) distal sinter apron terraces (see Guido and Campbell (2011) and Hamilton et al. (2019) for a detailed lithofacies and textural analysis of comparable sinters). Older samples of this study were inferred to have precipitated from circum-neutral pH, alkali-chloride thermal fluids, based on textural comparisons to active systems (cf. Cady and Farmer, 1996; Lynne, 2012; Hamilton et al., 2019). Many of the Pleistocene and older Holocene samples have undergone post-depositional acid overprinting with the infiltration of acidic steam condensate-derived corrosion, dissolution and acid leaching (e.g., Henneberger and Browne, 1988; Lynne and Campbell, 2006; Lyon et al., 2026; Rowe et al., 2025).

Five samples (GV-ng, TK-g, OK-g, A13, D50) are characterized as geyserite, forming in high-temperature proximal-vent areas. The geyserite lithofacies may be further categorized into spicular geyserite, which forms on the pool rim margin within the splash zone, and nodular/columnar geyserite forming away from the vent margin at the extent of the splash zone (Hamilton et al., 2019). GV-ng, a nodular geyserite, displays rounded nodules in a rosette-like pattern, mostly cemented together on the outer surface of the hand sample (Table 1). Internally, geyseritic laminae are concentrically rhythmic, radiating

Table 1
Macromorphology and micromorphology for studied samples.

Sample	Locality	Sinter lithofacies	Macromorphology	Micromorphology	Alteration/Diagenesis
GV-ng	Geyser Valley, Wairakei, NZ (−38.615688 176.084559)	Geyserite (nodular)	Clumped rounded nodules ~1-1.5 cm wide; wavy/merged bases; nodular to vertical concentric pseudocolumnar (~4 cm high); multifurcate branching; stacking of thicker on thinner columns; dark-coloured laminae between.	Concentric rhythmic outward nodules; even, dense, dark and light-coloured laminae (plan-view); vertical turbinate nodule column, stacking; dark-coloured fine-grained sediment between (cross-section); parasitic spikes atop nodule with cornices.	
TK-g	Te Kopia geothermal field, NZ (−38.410980 176.210393)	Geyserite (spicular)	Parallel acicular columns; branching spicules; densely clustered layered spicules (≤2.5 cm high, 500 μm to 3 mm wide); dense dark grey well-preserved interior.	Individual non-branching to branching spicules; convex radiating/fanning growth; fine dense to porous laminae in spicules; faint cornices and parasitic spikes (~250 μm thick).	Porosity and dissolution on outer portions of the geyserite digitate features (radiating fabric) and secondary porosity owing to strong acid alteration; samples' outer exterior has white powdery areas which were subjected to acidic hydrothermal steam alteration from the outside inwards.
OK-g	Orakei Korako, NZ (−38.479091 176.146482)	Geyserite (spicular)	Tight vertical/fan-shaped packed acicular spicules (~1.4 cm height); uniform fanning/botryoidal-type spicules; anastomosed spicules (~2.3 cm wide); densely silicified.	Bridging between individual spicules; a region of palisade fabric surrounds mid-temperature crenulated stromatolite; indicates cessation of vent; no clear parasitic spike texture.	Abundant primary, fenestral fabric enlarged to vugs due to acidic overprinting; extensive secondary porosity indicative of transition to acidic conditions.
A13[a]	Ohakuri, NZ (−38.38940 176.07890)	Geyserite (spicular)	Vent pool rim geyserite (30 cm thick, 1 m wide) with very fine branching anastomosed spicules (1-2 mm diameter); densely clustered spicules with light grey to brown interiors.	Spicules embedded in reticulated fine glassy silicified filaments (~1 μm diameter); stacked buff to orange-brown horizontal beds (3-8 mm thick); dark brown, densely stacked interior laminae of flat to moderately convex spicules.	Silica in spicules is either glassy and featureless, or brown and textured with moderate dissolution between laminae; filament silica is smooth; localised regions preserve silica forming 'dissolution ridges' with scattered clays.
D50[a]	Ohakuri, NZ (−38.39419 176.07447)	Geyserite	Vent pool rim geyserite with branched, anastomosing spicules; thin dark-coloured laminae between geyserite horizons.	Spicules surrounded by a network of fine filaments; parallel to moderately divergent geyserite columns (~2 mm high, ~1-1.5 mm wide); poorly preserved laminae with silver-grey to semi-transparent colouring.	Spicules and filaments surrouded by siliceous clay/silt; spicule laminae is typically silver-grey to glassy, in places bleached (intact but all textural details lost), in others partly dissolved.
WS-ct	Whangapaoa Spring, NZ (−38.363053 176.049875)	Conical tufted	Individual, finely laminated, cone shaped tufts; convex upward growth; closely-spaced; ≤1.2 cm high, ~1.5-2 mm wide.	Finely to moderately thick filamentous microbes; tangled groupings; string/ribbon-like extensions; web-like patterns; primary fenestral porosity; stacked wavy laminations; clotted peloidal fabric; network fabric.	
C75[a]	Ohakuri, NZ (−38.39178 176.06197)	Palisade fabric	~1.8 cm high thinly bedded palisade horizons; porosity evident between beds; wavy/climbing patterns in terracettes.	Coarsely filamentous microbes densely packed in vertical micropillar structures; repetitive vertical or flattened growth; mamillated patterns of filament growth in thick microbial mat.	Extensive silica encrustation around filaments; rare (diagenetic) quartz development among filaments (filaments appear unaffected by it); filaments altered by acidic conditions appear somewhat bleached.
C112[a]	Ohakuri, NZ (−38.39328 176.06261)	Palisade fabric	Thin laminae at top; porous, tuft/network-like webbing at bottom, extending perpendicularly into thick ~1 cm high vertical micropillar laminations; lenticular voids present (bubble mats).	Coarse perpendicular growth filaments packed within alternating density of laminae and small fenestrae; laminations overlie elongated pores; network/clotted fabrics, patchy diagenesis, iron filling, variable primary porosity preserved in several laminae; dark pigments to light-coloured horizons.	Extensive silica encrustation around filaments (light brown and clumpy), where altered by acidic conditions (evidenced by dissolution vugs lined by reddish-brown siliceous deposits) silica encrusting filaments is glassy and featureless; filament details are variably preserved.
044-1[a]	Ohakuri, NZ (−38.39144 176.06091)	Palisade fabric	Drill core palisade fabric with transition to marsh; thin laminae at bottom with porous network-like webbing overlain; extends perpendicularly into densely silicified marsh.	Coarse (~6.94 μm) to thin (~7.21-9.31 μm) filaments; flat, even to gently sloping palisade growth laminae horizons (~1 mm thick); peloids, desmids and plant material apparent; acidic overprinting; late influxes of silica precipitate as quartz and opal-A.	Extensive silica encrustation around filaments; filaments altered by acidic conditions, appear bleached and encrusting silica appears glassy, featureless; rapid quartz growth in palisade horizons destroys textural evidence of filaments.

(continued on next page)

Table 1 (*continued*)

Sample	Locality	Sinter lithofacies	Macromorphology	Micromorphology	Alteration/Diagenesis
NW-wp	Northern Waiotapu, NZ (−38.354348, 176.369334)	Palisade fabric	≤1.25 cm thick bedded palisade horizons with climbing/wavy patterns; primary porosity as small fenestral to spheroidal voids.	Densely filamentous vertical micropillar structures; clear coarse filamentous microbes; webbed filaments partially fill some primary fenestral porosity; rhythmic wavy laminations, some form crenulated stromatolitic textures; streamer fabric comprised of flattened filaments observed.	
OK-ss	Ohakuri, NZ (−38.38940 176.07890)	Palisade fabric	Palisade fabric buries high-temperature OK-g geyserite sample; apparent depositional acid overprinting; ~1 mm thick aggrading ripple-like laminae (terracettes).	Fluid-flow direction preserved in long, coarse filament molds; primary fenestral fabric throughout, linked to acid alteration.	Coarse filamentous cyanobacteria molds (i.e. not intact), with no distinct sheath or trichome component, with extensive 'build-up' of silica around filament structure. Red coloration to handsample indicating overprinting with Fe-oxidation.
Non-sinter sample					
OM3	Rosevelt Hot Springs, Utah, USA (38.468369 -112.869436)	colloform silica	Dense, pink silica with a knobby surface. Orpinent and realgar in As-rich domains.	Finely, evenly layered, silica banding; wavy to globular microscopic texture, with individual silica bands/layers with uniform thickness (contrasting stromatolitic texture).	

Note: [a]Sample descriptions from Ohakuri localties from Lyon et al. (2026). Terminology follows Walter et al. (1992, 1996) and Grey and Awramik (2020), and for digitate samples follows morphological subtypes sensu Sriaporn et al. (2020).

outward in nodular arrangements, with alternating more/less dense horizons (Fig. 1C). Samples TK-g, OK-g and A13 constitute spicular geyserite, with a macromorphology of densely and finely laminated, convexly oriented, needle-like (acicular), branched digitate features (Table 1). Microscopically, these samples occur as narrow vertical columns densely stacked together and containing convex dense laminae. Sample D50 shows no clear textural indication relative to its pool rim positioning. This geyserite sample is comparative to the rosette-like

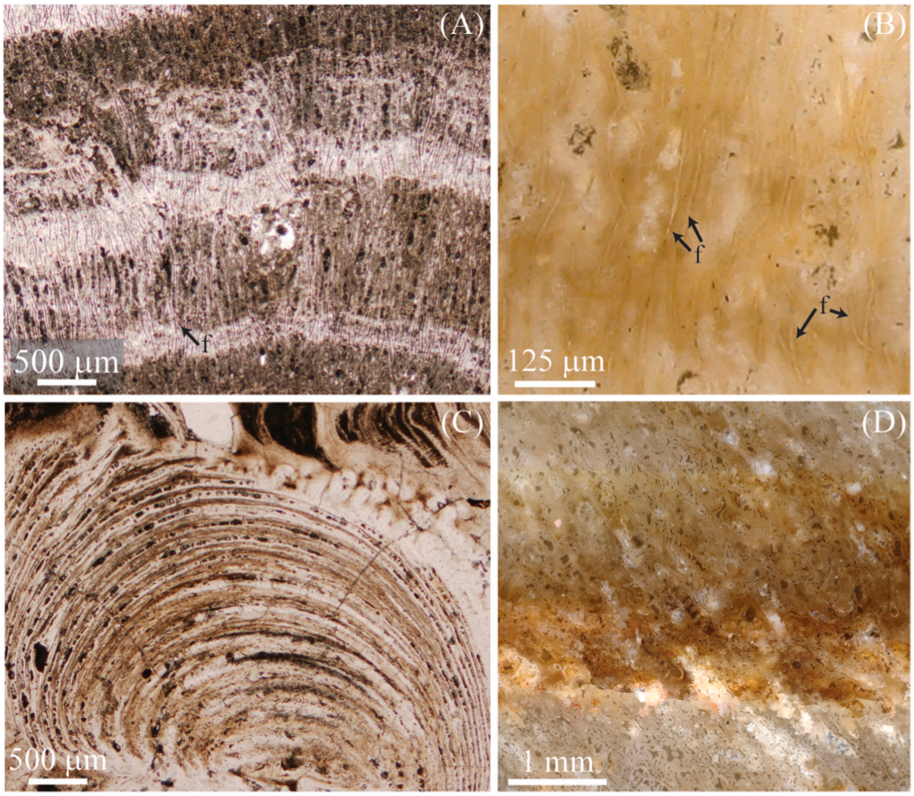

Fig. 1. Plane polarized transmitted light (A, C), and polarized reflected light (B, D) sample images from thin sections and epoxy mounts, respectively. (A) Palisade sinter texture from sample C75 illustrating the layered silica structure (darker porous layers are bracketed by white, low porosity layers) and columns of vertically aligned microbial filaments (f). (B) Residual pigments in sample NW-wp (wavy palisade texture), outlining silicified microbial filaments (f). (C) Nodular geyserite texture in sample GV-ng, demonstrating a microstromatolic growth habit inferred to result from the templated laminations of exopolymeric substance (EPS; cf. Handley et al., 2008). (D) Iron staining (red coloration) in palisade sinter sample (OK-ss) follows a horizontal fracture in the sample, which has undergone fumarolic alteration. (For interpretation of the references to colour in this figure legend, the reader is referred to the Web version of this article.)

nodules of GV-ng (e.g., Watts-Henwood et al., 2017), with an interior consisting of moderately divergent columns (Table 1).

The WS-ct sinter sample comprises individual, finely laminated, cone-shaped tufts grown convexly upward in the morphology of conical tufted sinter (Table 1). These tufts are closely spaced, with heights of ≤1.2 cm and widths of ~1.5-2 mm. Petrographically (plan-view thin section), WS-ct has finely to moderately thick (diameter) microbial filaments, indicative of shallow subaqueous, mid-temperature pools on the middle sinter apron (cf. Campbell et al., 2020; Guido and Campbell, 2011; Hamilton et al., 2019).

Palisade fabric samples (C75, C112, 044-1, NW-wp, OK-ss) consist of coarsely filamentous, silicified microbes that are densely packed in vertical micropillar structures, accumulating in stacked horizons constituting the palisade sinter fabric (Fig. 1A; Table 1). All these samples contain wavy laminations (Fig. 1A), with pigmentation concentrated around microbial filaments (Fig. 1B). In addition to the variable primary porosity in palisade samples, acidic overprinting is evident in some samples, observed as either patchy recrystallization, elongated pores/vugs or etched/empty voids (diagenetically altered porosity) in the Ohakuri (C75, C112, 044-1) and Orakei Korako (OK-ss) samples (Fig. 1D).

2.2. Analytical methods

2.2.1. X-ray diffraction

Bulk powder X-ray diffraction (pXRD) was conducted on chips of all samples to assess the occurrence of silica phases (opal A → quartz; cf. Lynne and Campbell, 2003; Lyon et al., 2026) that may correlate to variable XRF/XANES results. X-ray diffraction was conducted at the University of Auckland (UOA) on a PANalytical Empyrean diffractometer and a Rigaku Mini Flex II X-ray diffractometer using copper X-ray ($K\alpha_1$ [Å] wavelength = 1.54060 Å, $K\alpha_2$ [Å] wavelength = 1.54443 Å; Kα (mean) [Å] wavelength = 1.5418 Å). Scans were run from 5 to 70° 2θ with a 0.013° step size and 97 s/step integrated count time (Empyrean) and from 5 to 90° 2θ with a 0.02° step size and a scan speed of 1.25°/min (0.96 s/step; Rigaku).

2.2.2. Whole rock ICP-MS

Whole rock trace element analyses were conducted on 9 sinter samples (7 Holocene samples in addition to Ohakuri samples C112 and C75) in 2023 and 2026 at the Pheasant Memorial Laboratory, Institute for Planetary Materials (IPM), Okayama University (Misasa, Japan) (Nakamura et al., 2022). Samples were digested following established methods for "Group I″ elements (Makishima et al., 2009; Nakamura et al., 2022). Group I elements include: Li, Be, Na, Mg, Al, P, K, Ca, Sc, V, Cr, Mn, Fe, Co, Ni, Cu, Zn, Ga, Rb, Sr, Y, Cd, In, Cs, Ba, La, Ce, Pr, Nd, Sm, Eu, Gd, Tb, Dy, Ho, Er, Tm, Yb, Lu, Tl, Pb, Bi, Th, and U.

Sample chips visually representative of the bulk material were initially dissolved in a combination of $HClO_4$, HNO_3 and HF, and subsequently underwent dissolution in $HClO_4$, following standard methodology detailed in Yokoyama et al. (1999). Samples C75, GV-ng, WS-ct, NW-wp and OM3 were dissolved in duplicate. Prior to analysis, the Sm concentration was confirmed using a calibration curve based on 5-10% of the sample solution. Subsequently, a^{149}Sm spike was added. Details regarding the individual methods such as reagents, standards and spikes used in this study, are available in Nakamura et al. (2003, 2022, and references therein).

The compositions of major and minor elements (Na, Mg, Al, P, K, Ca, Sc, V, Cr, Mn, Fe, Co, Ni, Cu, Zn, and Ga) were determined by ICP-SFMS (sector field mass spectrometer; Thermo Fisher Scientific Element XR) after Makishima and Nakamura (2006). Trace element abundances were analyzed using ICP-QMS (quadrupole mass spectrometer; Thermo Fisher Scientific iCAP TQ) after Makishima and Nakamura (2006). Note that the analysis of TK-g was only completed on the ICP-QMS and is considered semi-quantitative, with up to 20% difference compared to ICP-SFMS analyses of the major and minor elements. Analyses that had a^{149}Sm/^{147}Sm below 2 (following addition of the spike) reflected exceptionally larger discrepancies and were discounted. Duplicate analyses were averaged for this work. Most duplicates demonstrated significant heterogeneity between analyses, reflecting trace element variability driven by textural complexity in these studied materials. In particular, reproducibility varies from 5 to 30% in unknowns compared to generally <5% in standards (Table S1).

Ohakuri samples A13 and D49 (same material as D50) were analyzed by commercial facilities at ALS (Australia Laboratory Services), Brisbane, Australia. Sample analysis was conducted on 5-7g of pulverized sample, ground in a tungsten-carbide ring mill at the University of Auckland. Trace elements (including REEs) were analyzed using the "four acid super trace analysis" procedure by ICP-MS (ALS Methods ME-MS61L and MS61L-REE). No whole rock analysis for archive sample 044 is available.

2.2.3. Synchrotron X-ray analysis

Synchrotron X-ray fluorescence (sXRF) maps and 2D Ga K-edge X-ray absorption near edge spectroscopy (XANES) maps were collected on the X-ray fluorescence microscopy beamline at the Australian Synchrotron on all 12 silica samples. To allow easier identification of key target areas on the texturally complex geologic samples, both sXRF and XANES analyses were acquired with a 2 μm-spot size focused through a KB mirror pair and recorded by a Maia 384-element silicon detector D-revision (Ryan et al., 2010). For clarity, we note that we distinguish the scan area (total 2D scan area) from the scan region (selected 2D region within the scan area targeting features of interest) and, in the case of XANES analysis, from XANES energy spectra (graph of X-ray absorption intensity versus energy). In the following sections, 'sXRF maps' refers specifically to compositional maps collected at an incident energy of 12.9 keV, whereas 'XANES maps' refers to maps collected at incident energies from 10.25 to 10.65 keV (see below for further details).

2.2.3.1. X-ray fluorescence (sXRF). sXRF scan areas were analyzed using a 2-5 μm step size and a 0.5-1 ms dwell time (depending on scan area size). For very high-resolution 2D scan areas, longer dwell times were utilized (up to 10 ms). sXRF mapping utilized a 12.9 keV incident beam energy. This energy was chosen to optimize Ga maps because: 1) this particular energy is well characterized on the XFM-beamline at the Australian synchrotron, and 2) for this analysis we were not focused on high energy X-rays (atomic masses heavier than Ga). Samples were oriented at 90° to the X-ray beam, passing through the Maia detector (Howard et al., 2020). The Maia detector has good resolution above Ca and can also provide qualitative elemental distributions down to Si; whereas elements lighter than Si cannot be detected due to absorption from detector Be windows. Synchrotron XRF data were processed on the Australian Synchrotron Computing Infrastructure (ASCI) using a dynamic analysis X-ray fitting procedure GeoPIXE v 7.7 (Ryan et al., 1990, 2015), resulting in quantitative elemental compositions for Si, S, K, Ca, Ti, Cr, Mn, Fe, Cu, Ga, and As. In processed 2D sXRF maps, each pixel contains a quantified chemical composition. Average compositions were compiled from regions within the larger sXRF maps (collected at 12.9 keV) that matched the smaller 2D XANES scan areas and regions, in order to provide internally consistent chemical analyses across both the sXRF and XANES datasets (see below).

2.2.3.2. X-ray absorption near edge spectroscopy. The XANES data were collected over defined 2D mapping areas (similar to the sXRF maps). The defined 2D scan area was analyzed 156 times, once for each energy step of the XANES analysis (from 10.25 to 10.65 keV). Each pixel of the finished 2D map therefore contains a complete XANES analysis. From this information, we can then compile an average XANES analysis over a region of interest with the larger scan area. XANES scan areas were defined by the larger sXRF maps, with a 0.5-2 μm step size and 1 ms dwell time (similarly with a single high resolution scan dwell time at 10

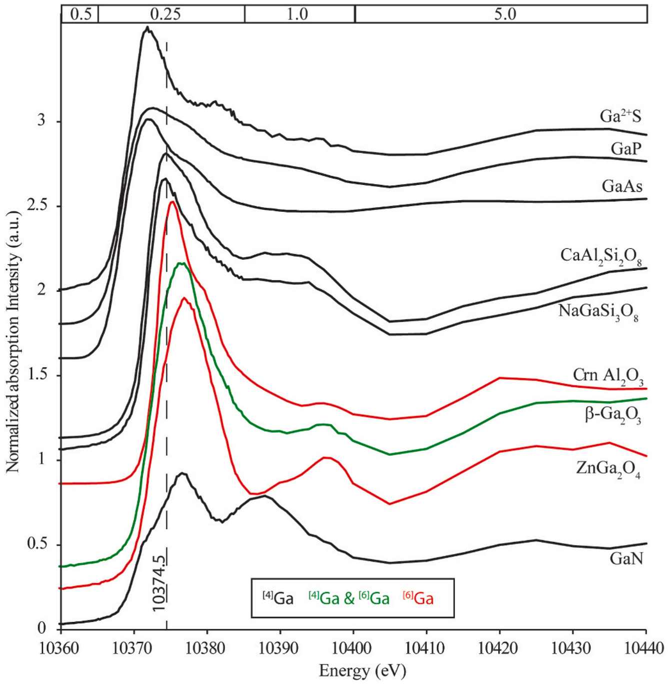

Fig. 2. Normalized Ga K-edge XANES spectra of standards analyzed during this study, including $^{[4]}$Ga (black) and $^{[6]}$Ga (red) and mixed $^{[4]}$Ga - $^{[6]}$Ga (green) coordination states. All standards have a Ga^{3+} oxidation state, with the exception of $Ga^{2+}S$. White line energy position for albite ($NaGaSi_3O_8$) and anorthite ($CaAl_2Si_2O_8$) at 10374.5 eV indicated as a point of reference. The energy step size (eV) is indicated in the bar at the top of the figure. (For interpretation of the references to colour in this figure legend, the reader is referred to the Web version of this article.)

ms). On average, dimensions of XANES scan regions were 0.5 × 0.3 mm, with the largest scan region 1.1 × 0.3 mm – the smaller scan areas compared to the sXRF areas were necessary because of the 156 repeated measurements needed to generate the 2D XANES maps. XANES standards analyzed include Ga_2O_3, GaP, GaS, and GaN, as well as the re-analysis of Ga-bearing standards from Mare et al. (2021), $ZnGa_2O_4$ (spinel), $NaGaSi_3O_8$ (albite), and also Al_2O_3 (corundum) and $CaAl_2Si_2O_8$ (anorthite), both doped with ~3000 ppm Ga (Fig. 2). Choice in standards reflects potential changes in both Ga oxidation state and coordination number, along with likely aluminosilicate and oxide structures.

From the XANES scan areas, XANES spectra were compiled from discrete regions. Regions were selected: 1) based on changes in rock textures and microbial features, derived from compositional mapping, or 2) directly from energy correlation diagrams. Scan regions varied in size, from 44 to 23416 pixels. Compiled energy spectra quality varied as a function of number of pixels and Ga concentration. XANES data were processed using the ATHENA program (Ravel and Newville, 2005). Exported XANES energy stacks were normalized and background corrected. Linear combination fitting (LCF) was conducted first using all available standards as pure fitting components, examining 84 potential combinations utilizing up to 3 different standards. The best fit was determined to be a mixture of standards anorthite, albite and spinel (Fig. 2). The structurally similar aluminosilicates, albite and anorthite, have very similar XANES spectra and both have tetrahedrally-coordinated Ga. As a result, only albite and spinel (octahedrally-coordinated Ga) were subsequently used as LCF end-members, providing a determination of the $^{[4]}$Ga and $^{[6]}$Ga proportions in analyzed sinter samples. Standard proportions of tetrahedral and octahedral Ga calculated from the LCF fitting were forced to sum to 1, noting that for a small number of fits this forcing resulted in poorer correlations. Proportions are reported as a percentage of the tetrahedrally-coordinated Ga. The fit range for the LCF was from −15 eV to +65 eV relative to the absorption edge. White line energy position, typically the highest intense peak located just above the absorption edge associated with coordination environment and bond lengths, was also determined using ATHENA (calculated as the energy corresponding to the maximum absorption intensity of a flattened XANES spectrum). Qualitative 2D compositional maps from the XANES scan areas at 10.65 keV were also created for Si, S, K, Ca, Ti, Mn, Fe, and Ga. Where possible, comparable regions were compiled from the 12.9 keV sXRF scan areas, to provide quantitative compositions correlating to the 2D XANES scan areas and regions.

2.2.4. Electron microprobe analysis

Backscatter electron (BSE) imaging and WDS X-ray maps were collected on selected samples at the Institute for Planetary Materials (IPM), Okayama University (Misasa, Japan) to support the synchrotron analyses, providing imaging and major element distributions. Analyses were conducted on a JXA-8530F field emission electron microprobe utilizing a 15 nA accelerating voltage, 100 nA beam current and 1 μm spot size.

3. Results

3.1. X-ray diffraction

Powder XRD of 12 sinter samples in this study demonstrate variability in silica phase structure between the siliceous samples. Silica phases are identified by their full width half max (FWHM) values and peak shapes (Lynne et al., 2007). Generally, Holocene samples (Gv-ng, OK-ss, WS-ct, NW-wp, OM3) are all opal-A (Fig. 3). TK-g and OK-g are

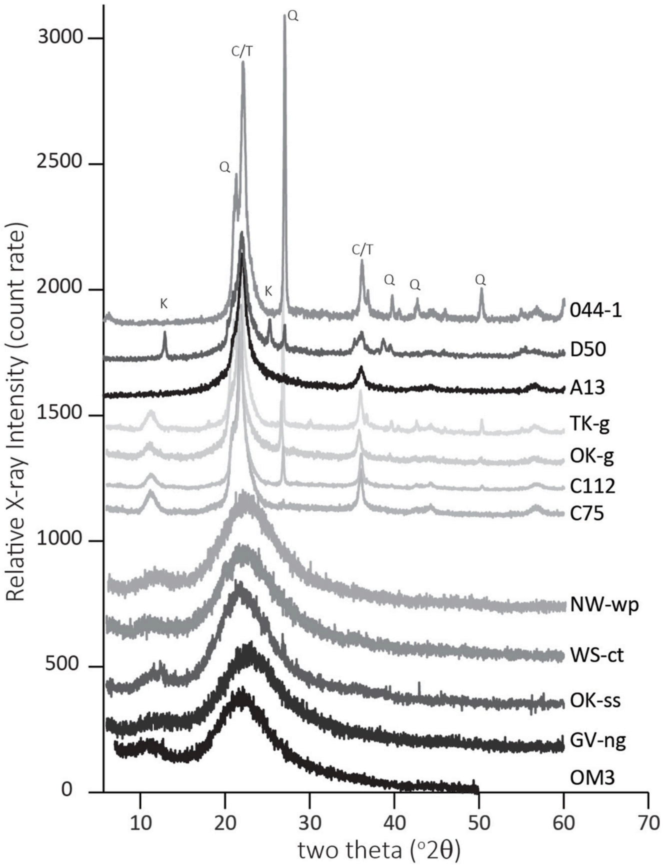

Fig. 3. X-ray diffraction results for sinter samples analyzed in this study. Results indicate two predominant silica polymorphs: opal-A and opal-CT (with variable quartz ± kaolinite). K = kaolinite, Q = quartz, C/T = cristobalite/tridymite.

Table 2
Selected elements from bulk compositions of samples.

Sample	GV-ng^{a}	OK-g	TK-g	D49	A13	C75^{a}	NW-wp^{a}	WS-ct^{a}	C112	OK-ss	OM3^{a}
Concentration (in ppm)											
Al	2494	8004	660	12600	4500	2340	92.8	3325	3876	18844	1422
K	1511	1788	280	800	1600	861	60.8	1729	481	2322	1795
Ca	2546	3423	102	1300	1600	964	712	1850	784	2487	935
Fe	228	782	194	9800	1100	95.0	46.9	363	938	2465	74.6
Ga	252	367	33.7	66.3	210	39.0	35.8	49.3	66.6	346	152
Rb	63.4	62.7	13.9	12.3	47.4	17.9	10.5	24.1	12.5	63.4	43.4
Al/Ga	9.9	21.8	19.6	190	21.4	59.7	4.76	67.1	58.2	54.5	9.33

Note: ^{a}Average compositions based on duplicate analysis at IPM. Analysis D49 is from the same location ad D50. Sample TK-g is semi-quantitative data (see text for further details). No bulk analysis is available for sample 044-1. Full chemical analyses available in Table S1.

both dominated by opal-CT and minor quartz, similar to Pleistocene samples from Ohakuri (C112, C75, A13, 044-1, D50).

3.2. *Whole rock chemistry*

Bulk compositions reflect the heterogeneity characteristic of sinter deposits (Jones and Renaut, 2003; Campbell et al., 2001, 2020). The full chemical compositions of all samples (excluding 044-1) are provided in Supplemental Table S1. Sample 044-1 is an archived core sample for which only proprietary assay data exist. For the remaining 11 samples, Ga concentrations vary from 18 to 305 ppm, with an average abundance of 138 ppm (Table 2). Fe and Al are moderately correlated to each other (0.65 Pearson correlation coefficient), while Fe is uncorrelated, and Al only weakly correlated to Ga (Table S2). Ga shows a strong positive correlation to Rb (0.94 Pearson correlation coefficient) across the samples of this study, while moderate positive correlations also were identified with Ca and K (Table S2). Among the samples investigated there is no obvious correlation between Ga concentration and sample age nor silica phases. Compositional variation is driven by differences in sinter textures. In particular, geyserite sinter has a higher average Ga content (186 ± 107 ppm) compared to lower temperature sinter textures (107 ± 133 ppm or 47 ± 14 ppm, when excluding the anomalously high OK-ss Ga content; Table 2). The Al:Ga is significantly lower (Al:Ga of 5-190; average of 47) and independent to Ga concentration, in contrast to other Ga resources (Foley et al., 2017). Sinter chemistry from New Zealand overlaps with that from Yellowstone National Park, USA, despite a larger range in composition at Yellowstone (Havig et al., 2021).

3.3. *sXRF*

Average compositions (from sXRF maps recorded at the incident energy of 12.9 keV) corresponding to each XANES scan area, as well as semi-quantitative compositions for the individual XANES scan regions, are reported in Table 3 and Table S3, respectively. Gallium is observed in all samples, with average compositions ranging from 7 to 1648 ppm Ga. In regions from XANES scans, a larger range in Ga is observed, with concentrations from 23 to 2338 ppm, reflecting internal heterogeneity on a micrometer-scale. Iron concentrations have an even greater range in composition, from 104 to 9307 ppm average compositions (XANES area), and from 53 to >35000 ppm in XANES scan regions. Silicon results are treated qualitatively because Si is at the lower limit of the Maia detector. There is generally a factor of 2 difference in Si, from 29 to 63 wt% in the scan areas. In the regions, Si broadly increases with Ga and decreases with Fe content.

The distribution of Ga highlights a range of distinct microscopic and macroscopic textures within the sinter/silica samples, consistent with prior observations of sinter textures (Gangidine et al., 2020; Nersezova et al., 2023; Lyon et al., 2026). These textures that are spatially highlighted by Ga are broadly grouped into three categories: 1) clear association with silicified microbes (microbial filaments; Fig. 4A); 2) affiliation with textures known, or suspected, to be produced from

Table 3
Average sXRF compositions (ppm; acquired at 12.9 keV) matching XANES scan areas.

Sample	Mount	Area^{a}	Si	S	K	Ca	Ti	Cr	Mn	Fe	Cu	Ga	As	Pixels	Area (mm^{2})
concentration (ppm)															
WS-ct	epoxy round	conical tuft	438080	4803	714	2180	217	25	181	356		173		2277	0.06
OM3	epoxy round	silica bands	615530	6051	1138	1440		12	137	104		570		52820	0.21
Tk-g	epoxy round	spicule	613177	5476	562	952	280	14	102	728		652		11100	0.28
GV-ng	epoxy round	spicule	556576	4131	1406	8289	304	20	155	257		1044	460	15096	0.38
NW-wp	epoxy round	palisade	605503	9245		2904	12	19	231	124	8.3	185		11286	0.28
OK-g	epoxy round	spicule	534950	4592	236	3074	43	16	48	269		534		6820	0.17
OK-ss	epoxy round	fluid	293776		443	2254	2398			5660		1648		36995	0.15
044-1	thin sect.	fluid	489420		332	1764	663	37.2	33.2	1501	50.8	45.3	2038	147492	0.59
A13	thin sect.	spicule	524518	3159	243	2636	13	27.9	111	127		174	7.4	104416	0.42
D50	thin sect.	spicule	501433	3449		1548	58	36	62.8	237		44	4.8	66990	0.27
C75	epoxy round	filaments	637431	6923	464	1459	48	19	37	162		463		2480	0.06
C75	thin sect.	filaments	492080		430	15509			44	331		86	2516	5530	0.02
C75	thin sect.	perp filament	491268	27	521	14543			59	314		87	2501	5530	0.02
C75	thin sect.	perp filament	506693		432	14036			66.5	326		94.4	2486	6867	0.03
C112	epoxy round	fluid	432443				726			9307	7	282		2652	0.07
C112	epoxy round	palisade	516898	4310	498	631	321	13		1697	5.7	83		2652	0.07
C112	epoxy round	plant mold	526803	5003	199	1123	139	20	37	982	20.9	197		17892	0.45
C112	thin sect.	fluid	449530	1891		746	320	31.7	45.9	1306		80.2	9.7	104218	0.42
C112	thin sect.	filaments	371913	1981		270		28.7		324	2.6	7.3	4.7	83080	0.33

Note:^{a}Area is a descriptor for the entire 2D XANES scan area.

biological processes even if microbial material is not identifiable (biofabrics, e.g., geyserite sinter textures; cf. Campbell et al., 2015; Guido et al., 2019, Fig. 4B); and 3) association with inferred abiotic processes (e.g. high-temperature silica precipitation or overprinting of primary fabrics by later fluids/gases; Fig. 4C). Capturing the contrasting spatial distributions of Ga (along with Fe), resulting from both primary sinter deposition and secondary (alteration/diagenesis), forms the basis for selecting XANES analysis areas.

3.4. Ga K-edge XANES

Seventy-five individual regions of interest were analyzed from 16 XANES map areas, covering the 12 distinct samples. White line energy positions calculated by ATHENA record a change of ~3 eV, from 10374.5 to 10377.4 eV overall (based on the smallest measured energy step size of 0.25 eV; Figs. 2 and 5; Table S3). In actively forming sinter (WS-ct), white line energy positions are highly restricted, with an average of 10374.6 ± 0.1 eV. Holocene-aged samples (GV-ng, OK-g, OK-ss, NW-wp, TK-g) record a greater variability in white line energy positions and are, on average, offset to higher energies (10375 ± 0.8 eV). Pleistocene (>16ka) aged, Ohakuri sinter sample (C112, C75, D50, 044-1, A13) white line energy positions are highly sample-dependent and show greater heterogeneity, with some samples identical to actively forming sinter (average 10375.2 ± 0.9 eV). The colloform opal sample (OM3) has a white line energy position that is also similar to actively forming sinter at 10374.5 eV. Corresponding to changes observed in the white line energy positions, we also observed changes in post-edge features. Most notably we see a broadening of the first absorption peak (white line), and a shift to higher energy for the peak B energy position (10392 to 10396 eV). Note that peak B decreases in normalized absorption with a shift to higher energy (Fig. 5).

From LCF models, the XANES scan regions highlight a compositional range between modelled end-member standards albite ($^{[4]}$Ga) and spinel ($^{[6]}$Ga) (all LCF are available in Table S3). Model fits also correlate to the change in white line energy position (Fig. 6). These two approaches are internally correlated as they are derived from the same XANES dataset. In subsequent discussion we refer only to the calculated proportions of tetrahedral Ga based on the LCF modelling, as it is the more statistically rigorous approach. For each XANES scan region, an average percentage of $^{[4]}$Ga (defined as $^{[4]}$Ga/[$^{[4]}$Ga + $^{[6]}$Ga] *100) is calculated from LCF modelled proportions of albite and spinel end-members. Although results span the entire compositional range, ~60% of the regions yielded 100 to 80% $^{[4]}$Ga, while 20% contained only 0 to 20% $^{[4]}$Ga, leaving only 20% of the regions to have between 20 and 80% $^{[4]}$Ga, suggesting an almost bimodal population distribution, although heavily weighted toward tetrahedral Ga. We subsequently refer to these three categories as "high" (100-80%), "intermediate" (80-20%), and "low" (20-0%) proportions of tetrahedral Ga. $^{[4]}$Ga-bearing sinter is the dominant component and volumetrically encompasses the bulk of the analyzed material. This material includes the distinctive microbial textures identified by Ga-enrichment (cf. Lyon et al., 2026). For the XANES regions containing an intermediate proportion of $^{[4]}$Ga, we note two distinct spatial distributions. First, several regions with intermediate proportions of $^{[4]}$Ga were identified spatially between distinct high- and low-proportion $^{[4]}$Ga regions and therefore likely represent a transition zone between the two end-members. Second, two of the sample areas have a Ga distribution suggesting inclusion of particles with an intermediate proportion of $^{[4]}$Ga (Fig. 7). The majority of regions composed of low proportions of $^{[4]}$Ga are associated with broad Ga enrichment, lacking textural evidence for microbial preservation (either observable silicified microbes, or inferred microbial textures; Fig. 1A–C). Only sample area of C112 preserves a low, but resolvable Ga enrichment along traces of microbial filaments, correlated to a low proportion of tetrahedral Ga (~5%). Two areas, also from sample C112, display small, isolated regions (particles) dominated by octahedral Ga, similar to those observed in the regions with an intermediate proportion of $^{[4]}$Ga (Fig. 7). Although we cannot completely rule out a contamination origin to the particles dominated by octahedral Ga, we note that alumina oxide, which could contain trace Ga, was only used as a final polish, with a 0.05 μm size fraction, and therefore is too small to explain the 50 μm particles. With the exception of the $^{[6]}$Ga-rich particles in Fig. 7C, in which Ga is correlated to Fe, none of the particles demonstrate an obvious correlation to elements measured by sXRF.

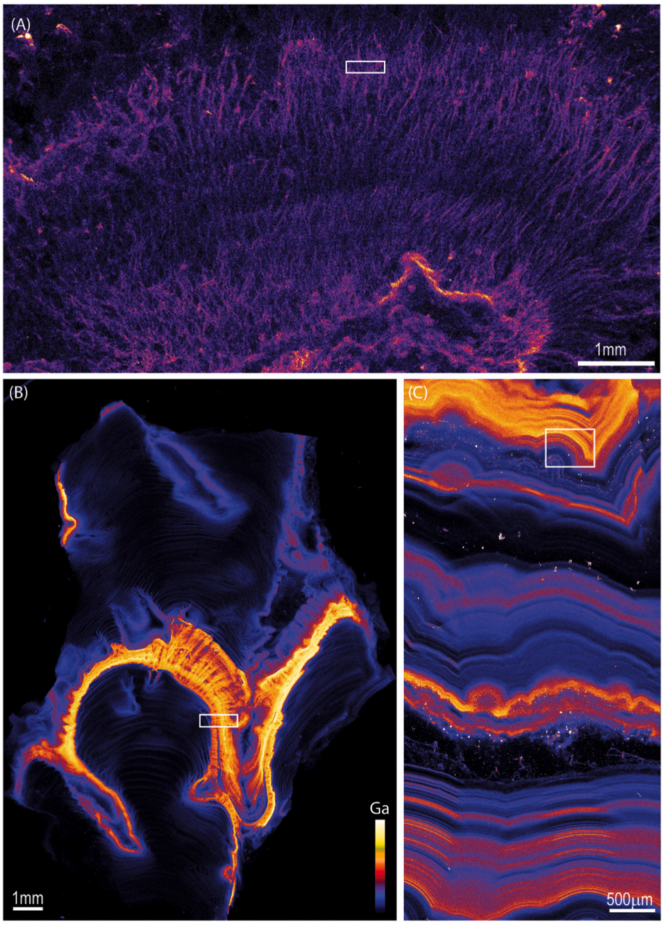

Fig. 4. Ga sXRF maps of Ga distribution associated with (A) silicified filamentous microbial material in C112 palisade sinter texture (B) inferred biofabric (e.g. EPS or biofilm, cf. Cady and Farmer, 1996), in geyserite sinter texture (GV-ng), and (C) colloform silica (OM3). Individual filaments are enriched in Ga in (A). Ga concentration shown by the scale bar in (B) is relative to each individual image, with warmer colors indicating higher concentrations. White boxes indicate XANES scan areas. (For interpretation of the references to colour in this figure legend, the reader is referred to the Web version of this article.)

3.5. Electron microprobe analysis

Electron microprobe analysis (EPMA) of sample OK-ss highlights the effects of hydrothermal overprinting. A low mean atomic number phase, identified on the BSE image, is correlated to elevated Fe and Al with lower Si within precipitates in a dissolution feature, compared to the surrounding sinter (Fig. 8). Distinct amorphous spheres of Si are also evident in this dissolution feature. No evidence from the BSE image exists to support the presence of Fe oxides (which would appear bright from the concentration of Fe) in this hydrothermally overprinted sample.

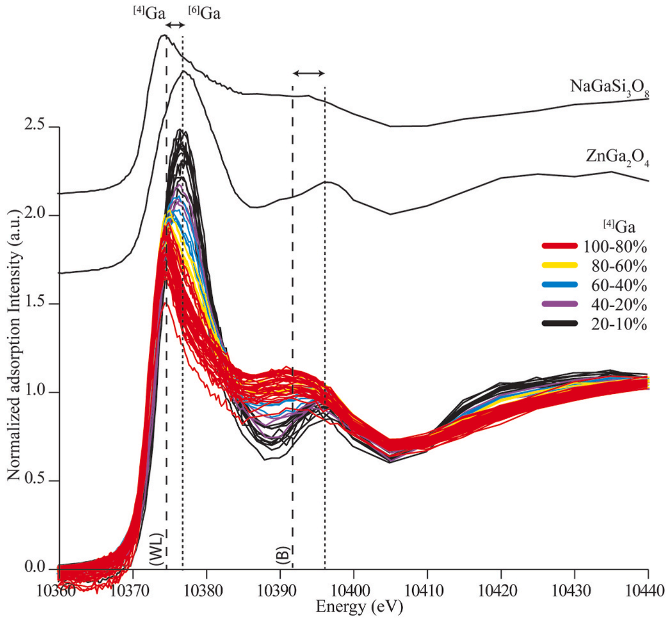

Fig. 5. Normalized and background-subtracted XANES energy spectra from mapped regions. $NaGaSi_3O_8$ (albite) and $ZnGa_2O_4$ (spinel) standards provide reference for key shifts in white line energy positions and post-edge features. Samples are color-coded based on the proportion of Ga-albite ($^{[4]}$Ga) in 20% increments to highlight the shift in white line energy positions (WL) and B peak energy positions (B) associated with coordination change. (For interpretation of the references to colour in this figure legend, the reader is referred to the Web version of this article.)

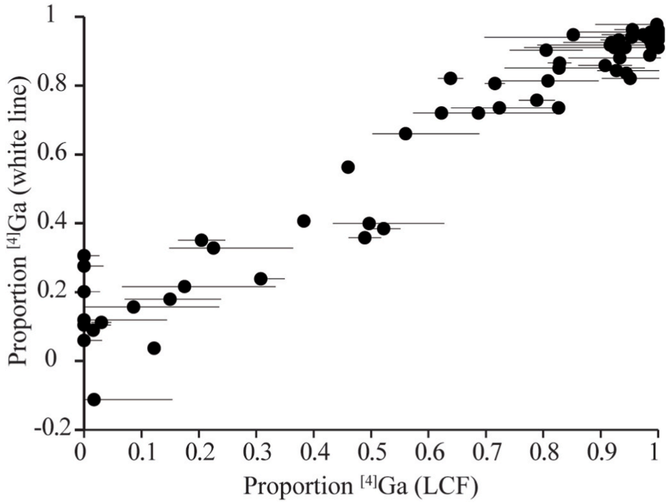

Fig. 6. Comparison of the proportion of tetrahedral $^{[4]}$Ga (with the remaining fraction attributed to $^{[6]}$Ga) from linear combination fitting (LCF) and from white line energy positions. Error bars (LCF) are calculated in ATHENA. One analysis from sample C112 has a white line energy position greater than the spinel model end-member by 0.3 eV, producing a negative calculated proportion of $^{[4]}$Ga. This likely results from imprecision in the estimation of the white line position from ATHENA, which is based on the maximum adsorption intensity rather than a more rigorous peak fitting process.

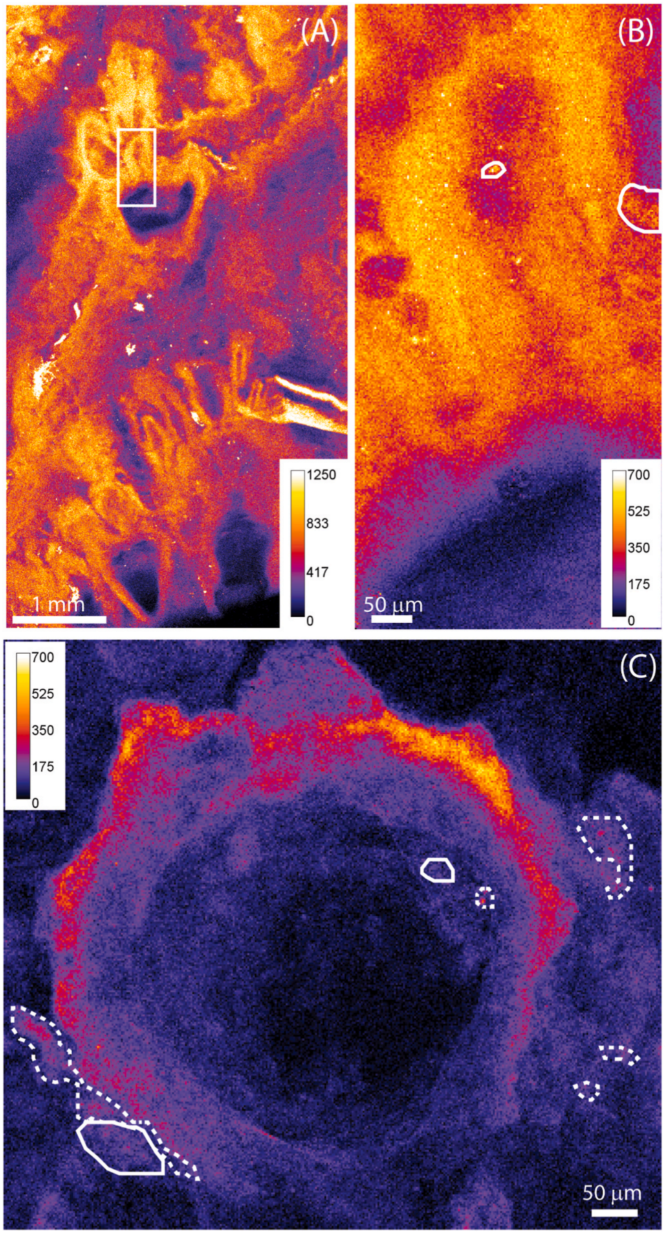

Fig. 7. Gallium distribution and particle-like distribution of high coordination number (CN) Ga in geyserite sinter (A-B; TK-g) and in a silicified plant mold (C; C112). Recorded incident energy for maps: A – at 12.9 keV; B and C at 10.65 keV. (A) Low resolution sXRF scan demonstrates compositional heterogeneity around geyserite spicules. The white box outlines the scan area in (B). (B) Gallium high 2D spatial resolution map. White circled regions indicate elevated a lower proportion of tetrahedral Ga (65%) compared to the rest of the scan region with tetrahedral Ga proportions of 85-95%. (C) Plant mold (95% $^{[4]}$Ga) with particles containing low proportions of tetrahedral Ga enclosed within solid white (15% $^{[4]}$Ga) and dashed (30% $^{[4]}$Ga) lines. Percentages indicated adjacent to spectra are the calculated percentage of $^{[4]}$Ga ($^{[4]}$Ga/[$^{[4]}$Ga + $^{[6]}$Ga]). Gradients are Ga concentrations (ppm).

4. Discussion

4.1. Gallium coordination in sinter

Depositional paleoenvironments for sinter samples are interpreted from textures following a well-established lithofacies model based on modern examples, indicating primary textures formed from circumneutral alkali chloride fluids from ~90 °C to <45 °C (e.g., Cady and Farmer, 1996; Guido and Campbell, 2011; Lynne, 2012; Hamilton et al., 2019). Although the exact environment of formation is unknown for the colloform opal material (sample OM3), its close spatial relationship to sinter deposits in the Roosevelt Hot Springs (Lynne et al.,

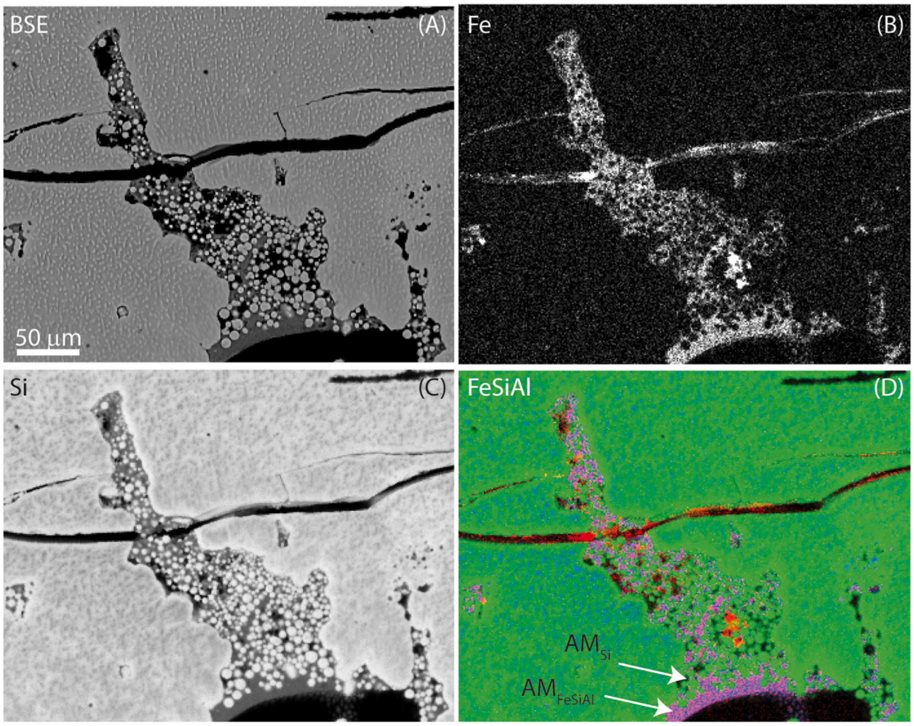

Fig. 8. Electron microprobe BSE (A) and WDS X-ray maps (B-D) of overprinting hydrothermal fluid precipitates in sample OK-ss. WDS Fe (B), Si (C) and FeSiAl (RGB) x-ray maps highlight the distinction between amorphous silica spheres (AM$_{Si}$) and the inferred amorphous Fe–Si–Al rich phase (AM$_{FeSiAl}$; dark grey region on the BSE image(A)). Note the absence of identifiable bright minerals in the Fe-rich regions of the BSE image, supporting the absence of a microcrystalline Fe oxide phase.

2005) suggests similar composition fluids, albeit at higher temperatures (Hedenquist and Arribas, 2017). Despite the range in inferred temperature of sinter deposition, and heterogeneous Ga distribution (Fig. 4) and variable sinter composition (Table 2; Table S3), Ga is tetrahedrally coordinated in all primary (i.e. depositional) sinter textures. In Si-bearing fluids with a pH > 3, Ga-EXAFS and NMR indicate a predominance of Si–O-Ga bonds in tetrahedral coordination (Pokrovski et al., 2002), consistent with our observations of Ga in sinter primary textures of this study. Gallium is also predicted to be adsorbed in tetrahedral environments on amorphous silica (Pokrovsky et al., 2004). Thus, Ga coordination preserved in primary textures of sinter deposits is consistent with fluid compositions, suggesting no significant changes to silica coordination during silica polymerization/precipitation and adsorption. Sinter samples investigated in this study also record the occurrence of silica phases from opal-A to opal-CT (with scattered quartz; Fig. 3). Despite the variability of silica phases present, Ga is still primarily tetrahedrally coordinated. This finding is consistent with observations that Ga can maintain its spatial association with primary

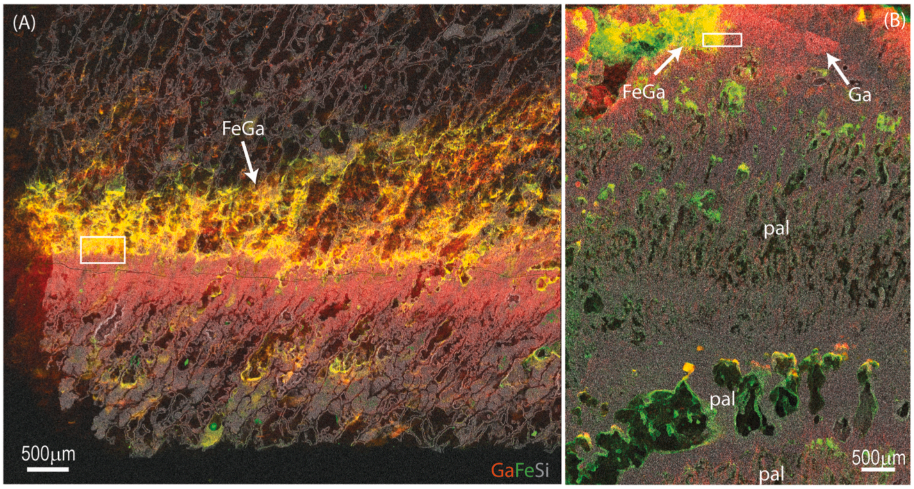

Fig. 9. sXRF maps recorded at an incident energy of 12.9 keV of (A) OK-ss and (B) C112 highlighting chemical changes associated with fluid infiltration and alteration. Composite images of Ga (red), Fe (green) and Si (grey). Addition of Fe and Ga-bearing fluids (yellow) creates a distinct distribution of trace metals compared to primary deposition patterns (e.g. Fig. 4). White boxes indicate XANES scan areas in Fig. 11. (For interpretation of the references to colour in this figure legend, the reader is referred to the Web version of this article.)

textures (e.g., microbial fabrics) in sinter through diagenesis, even in silica that has completely recrystallized to quartz (Nersezova et al., 2024; Lyon et al., 2026). These results suggest that Ga is not co-precipitated with a nano- or micro-oxide phase within the amorphous silica, nor is it electrostatically attracted to the amorphous silica since Ga in this form would be expected to be expunged during silica maturation, resulting in reduced concentrations and Ga redistribution (Table S1; Sanchez-Yanez et al., 2017). Instead, the retention of Ga (both its distribution and concentration) is similar to Sb and Cu in sinter, which appear to be incorporated into the silica structure early in sinter formation (Sanchez-Yanez et al., 2017).

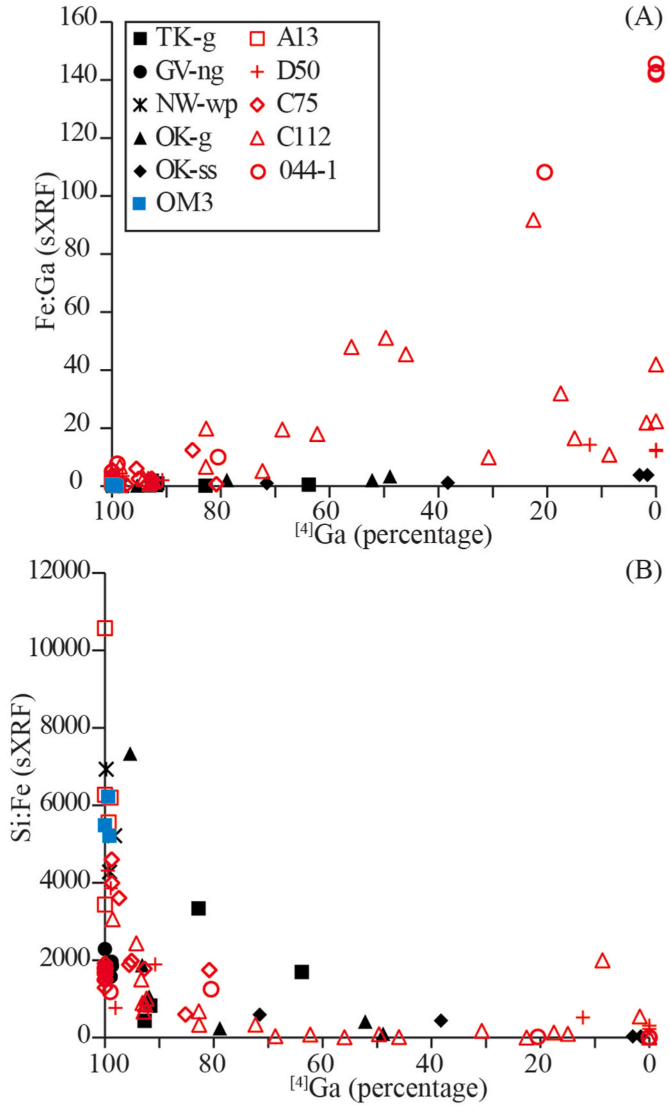

Fig. 10. (A) Fe:Ga and (B) Si:Fe from sXRF versus calculated proportion of tetrahedral Ga, based on the proportion of modelled albite from LCF. Note the significant increase in Fe:Ga with decreasing proportions of $^{[4]}$Ga in Pleistocene samples from Ohakuri (open symbols) resulting from increasing Fe content (Table 3). Fe:Ga enrichment in Holocene samples (e.g. OK-ss) is minimal as a result of significant enrichment in both Ga and Fe (Table 3). Si:Fe decreases with decreasing proportions of $^{[4]}$Ga in all samples and reflects both lower Si and higher Fe.

4.2. *Effect of fluid overprinting on gallium coordination*

Following primary silicification of microbial components in sinters, secondary fluids have the potential to remobilize elements and/or introduce new chemical constituents into the system (i.e. adding chemical complexity) – essentially erasing pre-existing, primary chemical distribution signatures (Fig. 9; Hamilton et al., 2017; Rowe et al., 2025; Lyon et al., 2026). In the case of Ga, in addition to the textural modifications, in some cases we also note a respective change in the Ga coordination, from $^{[4]}$Ga to $^{[6]}$Ga (Fig. 5). This anomalous coordination of Ga may appear texturally as either discrete or diffuse in nature, and therefore may reflect multiple processes/products. A comparison between the semi-quantitative chemistry for the XANES scan regions and the calculated proportion of tetrahedral Ga highlights a negative correlation between the proportion of $^{[4]}$Ga and Fe:Ga, and a positive correlation between the proportion of $^{[4]}$Ga and Si:Fe (Fig. 10). Element ratios are used here to address relative chemical variability in a micro-spatial context. It is important to note that Si:Fe is a function of both variables – as Fe increases, Si decreases. However, Si:Fe is more strongly dependent on Fe, which has an overall significantly greater variability in composition. Similarly, Fe:Ga is more strongly correlated to Fe ($R^2 = 0.71$) than to Ga ($R^2 = 0.03$). Interestingly, there appears to be multiple distinct correlations between Fe:Ga and Ga coordination, with the highest Fe:Ga present in Ohakuri sinter samples dominated by octahedral Ga (Fig. 10). Clearly the range in geothermal fluid compositions is able to influence Ga coordination environments, with the key ingredient being the addition of Fe (Table S3).

The correlation of Fe and changing Ga coordination numbers to fluid overprinting is also evident when considering the spatial distribution of chemical components. The 456-year-old Orakei Korako “Sinter Island” site has undergone significant hydrologic change resulting in alteration of primary textures owing to acidic steam condensate passing through the deposit (Lynne et al., 2007). This local overprinting by acidic fluids is reflected in hand sample and petrographically by the reddish coloration, likely associated with Fe oxidation (Fig. 1D; Table 1). However, there is no evidence from XRD results (Fig. 3) or backscatter electron imaging/WDS X-ray mapping (Fig. 8) to indicate the presence of Fe oxide precipitates. Additionally, coarse, thickened, filament molds lacking distinctive trichomes and sheaths are a result of dissolution and reprecipitation of silica, consistent with XRD evidence for minor quartz and a sharpening and slight shift to lower 2θ of the X-ray peak position (Fig. 3; cf. Lynne et al., 2007). The filament molds lack a distinctive trace element enrichment, commonly observed in unaltered microbial filaments (e.g., Nersezova et al., 2024; Lyon et al., 2026). However, a broad region of Ga enrichment is correlated to denser silica, with a clear distinction between it and a region of Fe + Ga enrichment (Fig. 9). 2D XANES area scans of this contact clearly highlights the change in Ga coordination, decreasing from 75 to 50% $^{[4]}$Ga associated with the Fe-overprinting, however the distribution of Ga enrichment within these regions does not align perfectly to Fe enrichment (Fig. 11). Similarly, in the Ohakuri sinter, with documented overprinting by several distinct fluids (Lyon et al., 2026), a clear spatial distinction correlated to changing Ga coordination ($^{[4]}$Ga decreasing from 95 to 25%) in sinter is observed between inferred secondary Ga-rich and Fe–Al-Ga fluids (Figs. 9 and 11), therefore highlighting the importance of fluid chemistry on Ga coordination. Dissolution vugs in the Ohakuri sinter are also observed to be lined with Fe–Al-Ga-rich silica precipitate and, in places, sulfur (Table 1; Lyon et al., 2026), pointing to a highly acidic overprinting fluid that corresponds to the predominantly octahedral Ga coordination in sinter. These observed correlations are supported by investigations in Ga coordination in aqueous fluids. Although Ga in aqueous fluids is octahedrally bound in the absence of silica (Pokrovski et al., 2002), despite the high Fe and Al and lower Si, Si remains a major

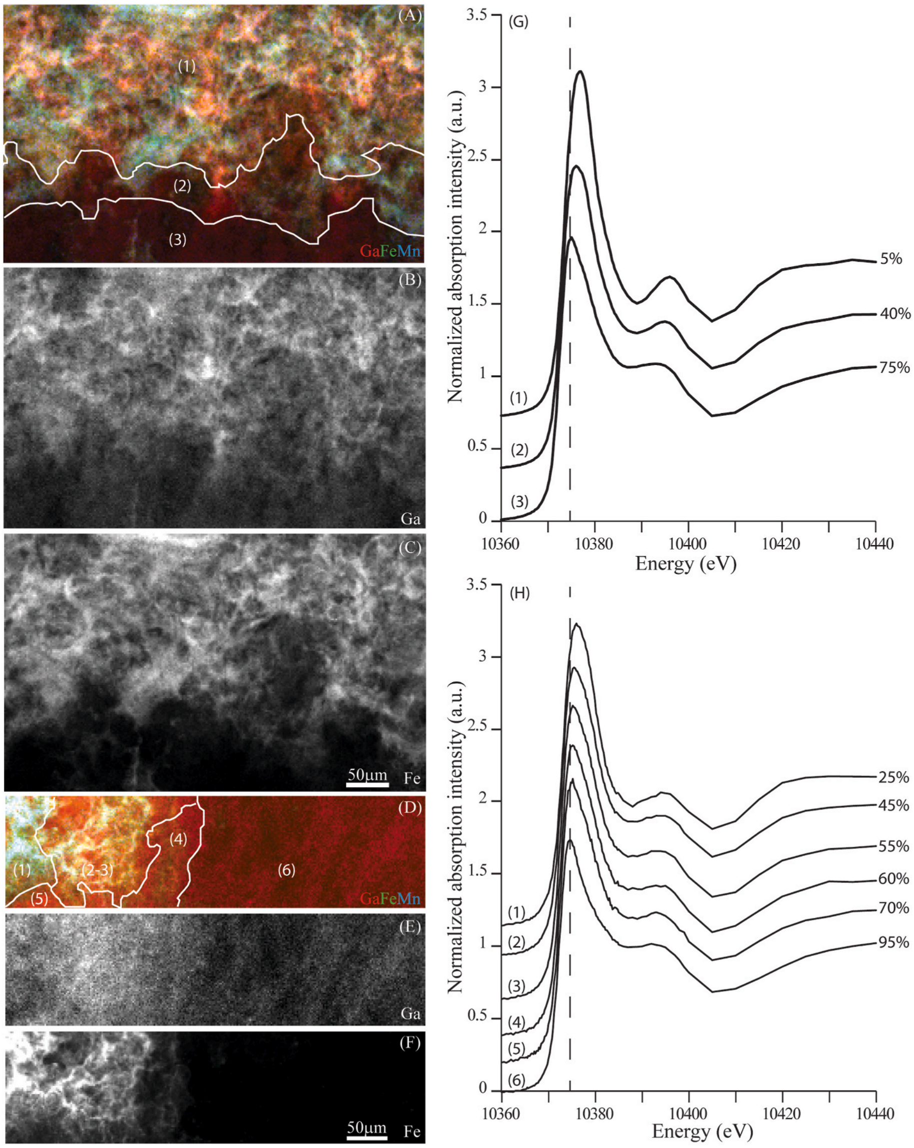

Fig. 11. XANES scan regions for (A-C) OK-ss and (D-F) C112. GaFeMn (RedGreenBlue) composite elemental maps from XANES scans at 10.65 keV. (A) and (D) are subdivided based on the calculated proportion of tetrahedral Ga of each XANES region. In particular, note the correlation between the Fe X-ray maps (C) and (F) and zones of lower proportions of $^{[4]}$Ga. Moreover, although Ga-enrichment in (B) and (E) is broadly correlated to zones of lower $^{[4]}$Ga, this Ga enrichment is less distinctive than in observed variations in Fe enrichment in (C) and (F). XANES energy spectra in (G) and (H) correspond to numbered regions in (A) and (D), respectively. Percentages indicated adjacent to spectra are the calculated percentage of $^{[4]}$Ga ($^{[4]}$Ga/[$^{[4]}$Ga + $^{[6]}$Ga]).

component in the overprinting fluids (Table 3). While as previously discussed, Ga is predominantly in tetrahedral coordination in circum-neutral pH fluids containing Si, there is an observed shift to octahedral coordination (i.e. GaO_6 octahedron bound to silica tetrahedron) under strongly acidic conditions ($pH < 3$; Pokrovski et al., 2002), consistent with our observations of fluid overprinting in active, volcano-tectonic geological settings such as the TVZ.

The measured change from tetrahedral to octahedral coordination of Ga in sinter may mirror the process of Ga redistribution and enrichment in lateritic bauxite deposits, where extreme weathering, typically in tropical climates, remobilizes Ga that is primarily stored in aluminosilicates, and thus frees it to be adsorbed to metal oxides (Qi et al., 2023). The results of our study on sinter suggest that as similar remobilization would likely accompany a change to an octahedral coordination environment. It is important to note that from available data we cannot distinguish whether Ga is adsorbed on the surface of precipitates or if it replaces elements in mineral structures. In contrast to inferred tetrahedral adsorption on amorphous silica, Ga is adsorbed octahedrally on carbonates and manganese oxides (Pokrovsky et al., 2004). If Ga adsorption on Fe oxide is similar to that of Mn oxides (Pokrovsky et al., 2004), then both processes may promote octahedral coordination in/on Fe-rich precipitates from overprinting high-metal content hydrothermal fluids. Alternatively, if Ga^{3+} replaces octahedral Fe^{3+} in Fe oxide, a similar change to octahedral coordination would be predicted. This method of Ga enrichment is distinct to that reported by Crump (1995), who suggested that Ga enrichment in geothermal muds in New Zealand resulted from Ga replacing Al in aluminosilicate minerals (kaolinite; Crump, 1995). Thus, it is the overprinting by acidic hydrothermal fluids, potentially coupled with the availability of metal oxides as adsorption sites, that seems to be primarily responsible for the transition of Ga from tetrahedral to octahedral coordination preserved in the sinter samples.

5. Conclusions

Gallium is heterogeneously distributed within sinter. Locally, the concentration of Ga observed in this study reaches concentrations up to

~1600 ppm, comparable to prior studies on Ga in sinter reporting concentrations up to 1500 ppm (Nersezova et al., 2024). Despite these spatially patchy high concentrations, the heterogenous distribution of Ga results in average concentrations ranging from 18 to 311 ppm, comparable to Ga levels found in other geothermal settings (Yellowstone National Park; Havig et al., 2021) and in other key Ga reservoirs globally (Foley et al., 2017; Lu et al., 2017). In all sinter samples of our study, Ga maintains a +3 charge, consistent with most occurrences of Ga in nature (Frick et al., 2000). In primary sinter textures and colloform opal associated with precipitation from alkali-chloride circum-neutral pH fluids, Ga is tetrahedrally-coordinated, with XANES suggesting a similar structure to aluminosilicate minerals (i.e., feldspars) likely represented by the Si–O-Ga bonding environment.

Fluid chemistry plays a key role in dictating changes in Ga chemical behavior in hydrothermal fluids and sinter. Secondary overprinting by inferred low pH and high Fe fluids result in a transition from tetrahedral to octahedral Ga coordination in sinter, with the potential addition of an X-ray amorphous Fe-rich phase into the pore spaces, whereas low Fe:Ga and high Si:Fe favors $^{[4]}$Ga. Importantly, all samples with a high Fe:Ga are dominated by spinel-like, $^{[6]}$Ga, but not all $^{[6]}$Ga regions have a high Fe:Ga. The mechanism by which $^{[6]}$Ga is bound in the secondary precipitates from low-pH, high Fe fluid is unclear; however, following from the experiments of Pokrovsky et al. (2004), adsorption onto Me-oxide phase(s) is likely. The co-occurrence of $^{[4]}$Ga and $^{[6]}$Ga in the studied hot spring sinter samples therefore provides a unique fingerprint for diagenetic processes that result in the alteration of primary geologic textures and the potential redistribution and enrichment of economically important metals.

Funding

Funding for this work comes from a RSNZ Marsden Fund grant (24-UOA-206; MR, KC).

CRediT authorship contribution statement

M.C. Rowe: Conceptualization, Funding acquisition, Investigation, Writing – original draft. **K.A. Campbell:** Funding acquisition, Resources, Writing – original draft. **D.A. Stallard:** Investigation, Writing – original draft. **B. Lyon:** Investigation, Resources, Writing – review & editing. **A. Langendam:** Investigation, Methodology, Writing – review & editing. **E. Kalinina:** Investigation, Writing – review & editing. **M. Yamanaka:** Investigation, Writing – review & editing. **R. Tanaka:** Investigation, Writing – review & editing. **T. Christopher:** Investigation, Writing – review & editing. **S.W. Ruff:** Resources, Writing – review & editing. **E. Nersezova:** Investigation. **T. Ota:** Investigation. **A. Hamilton:** Writing – review & editing.

Declaration of competing interest

The authors declare that they have no known competing financial interests or personal relationships that could have appeared to influence the work reported in this paper.

Acknowledgements

We acknowledge the numerous landowners who have granted permission over the 20+ years of access and sample collection including: J. Richards, A. Leinhart, C. and P. Gibson, I. Roe, and the Porter family. We thank Michelle Phillips and the Ngāti Tahu-Ngāti Whaoa Runanga Trust and the New Zealand Department of Conservation (DoC) for permission to access and study Te Kopia and the northern Waiotapu geothermal sites. For access to Ohakuri and Roosevelt Hot Springs we thank Zedex Gold, Ltd. and Larvotto Resources, Ltd., and R. Andrews of PacifiCorp. The authors acknowledge the Australian Synchrotron (AS241/XFM/21025) for providing beam time and technical support. Collaboration between Auckland and the Institute of Planetary Materials (IPM), Okayama University is possible through a continued 'International Joint Research' project issued by the IPM. This manuscript was improved by the comments from two anonymous reviewers.

Appendix A. Supplementary data

Supplementary data to this article can be found online at https://doi.org/10.1016/j.apgeochem.2026.106961.

Data availability

All data is available in the supplementary files.

References

Burton, J.D., Culkin, F., Riley, J.P., 1959. The abundances of gallium and germanium in terrestrial materials. Geochem. Cosmochim. Acta 16, 151–180.

Cady, S.L., Farmer, J.D., 1996. Fossilization processes in siliceous thermal springs: trends in preservation along thermal gradients. In: Bock, G.R., Goode, J.A. (Eds.), Evolution of Hydrothermal Ecosystems on Earth, vol 202. John Wiley & Sons, Ltd., pp. 150–173. https://doi.org/10.1002/9780470514986.ch9

Campbell, K.A., Guido, D.M., Gautret, P., Foucher, F., Ramboz, C., Westall, F., 2015. Geyserite in hot-spring siliceous sinter: window on Earth's hottest terrestrial (paleo) environment and its extreme life. Earth Sci. Rev. 148, 44–64.

Campbell, K.A., Nicholson, K., Lynne, B.Y., Browne, P.R.L., 2020. 3D anatomy of a 60-year-old siliceous hot spring deposit at Hipaua-Waihi-Tokannu geothermal field, Taupo Volcanic Zone, New Zealand. Sediment. Geol. 402. https://doi.org/10.1016/j.sedgeo.2020.105652.

Campbell, K.A., Sannazzaro, K., Rodgers, K.A., Herdianita, N.R., Browne, P.R.L., 2001. Sedimentary facies and mineralogy of the late Pleistocene Umukuri silica sinter, Taupo Volcanic Zone, New Zealand. J. Sediment. Res. 71 (5), 727–746.

Chen, F., Liu, F., Liao, B., Wang, J., Liao, C., Jiang, T., Zhang, J., Wang, H., Zhang, T., Zhou, 2025. Selective separation and recovery of gallium and germanium from complex polymetallic sulfate solutions. Miner. Eng. 234, 109758. https://doi.org/10.1016/j.mineng.2025.109758.

Crump, M.E., 1995. A new source of gallium – geothermal muds. PACRIM Congress 1995, Auckland, New Zealand, 19-22 November 1995. In: Mauk, J.L., St George, J.D. (Eds.), Proceedings of the 1995 PACRIM Congress; Organised by the Australasian Institute of Mining and Metallurgy [Proudly Sponsored by Macraes Mining Company Limited]. The Institute, Carlton, Vic.

Foley, N.K., Jaskula, B.W., Kimball, B.E., Schulte, R.F., 2017. Gallium. Gallium, chap. H of. In: Schulz, K.J., DeYoung Jr., J.H., Seal II, R.R., Bradley, D.C. (Eds.), Critical Mineral Resources of the United States—Economic and Environmental Geology and Prospects for Future Supply. U.S. Geological Survey Professional Paper 1802, pp. H1–H35. https://doi.org/10.3133/pp1802H.

Frick, R., Kosslick, H., Lischke, G., Richter, M., 2000. Incorporation of gallium into zeolites: syntheses, properties and catalytic application. Chem. Rev. 100, 2303–2405.

Gangidine, A., Havig, J.R., Fike, D.A., Jones, C., Hamilton, T.L., Czaja, A.D., 2020. Trace element concentrations in hydrothermal silica deposits as a potential biosignature. Astrobiology 20 (3). https://doi.org/10.1089/ast.2018.1994.

Goldschmidt, V.M., 1937. The principles of distribution of chemical elements in minerals and rocks. J. Chem. Soc. 655–673.

Grey, K., Awramik, S.M., 2020. Handbook for the study and description of microbialites. In: Geological Survey of Western Australia, Bulletin, vol. 147, p. 278. Perth.

Guido, D., de Barrio, R., Schalamuk, I., 2002. La Marciana Jurassic sinter: implications for exploration for epithermal percious-metal deposits in Deseado Massif, southern Patagonia, Argentina. Appl. Earth Sci.: Trans. Inst. Min. Metall., Sect. B 111 (2), 106–113. https://doi.org/10.1179/aes.2002.111.2.106.

Guido, D.M., Campbell, K.A., Foucher, F., Westall, F., 2019. Life is everywhere in sinters: examples from Jurassic hot-spring environments of Argentine Patagonia. Geol. Mag. 156, 1631–1638. https://doi.org/10.1017/S0016756819000815.

Guido, D.M., Campbell, K.A., 2011. Jurassic hot spring deposits of the Deseado Massif (Patagonia, Argentina): characteristics and controls on regional distribution. J. Volcanol. Geoth. Res. 203, 35–47.

Hagvall, K., Persson, P., Karlsson, T., 2014. Spectroscopic characterization of the coordination chemistry and hydrolysis of gallium(III) in the presence of aquatic organic matter. Geochem. Cosmochim. Acta 146, 76–89.

Hamilton, A., Campbell, K., Rowland, J., Browne, P., 2017. The Kohuamuri siliceous sinter as a vector for epithermal mineralisation, Coromandel Volcanic Zone, New Zealand. Miner. Deposita 52 (2), 181–196.

Hamilton, A.R., Campbell, K.A., Guido, G.M., 2019. Atlas of siliceous hot spring deposits (sinter) and other silicified surface manifestations in epithermal environments. Lower Hutt (NZ): GNS Sci. 56. https://doi.org/10.21420/BQDR-XQ16. GNS Science report 2019/06.

Handley, K.M., Turner, S.J., Campbell, K.A., Mountain, B.W., 2008. Silicifying biofilm exopolymers on a hot-spring microstromatolite: templating nanometer-thick laminae. Astrobiology 4. https://doi.org/10.1089/ast.2007.0172.

Havig, J.R., Kuether, J.E., Gangidine, A.J., Schroeder, S., Hamilton, T.L., 2021. Hot spring microbial community elemental composition: hot spring and soil inputs and the transition from biocumulus to siliceous sinter. Astrobiology 21 (12). https://doi.org/10.1089/ast.2019.2086.

Hedenquist, J.W., Arribas, R.A., 2017. Epithermal ore deposits: first-order features relevant to exploration and assessment. In: Mineral Resources to Discover, 1, pp. 47–50.

Henneberger, R.C., Browne, P.R.L., 1988. Hydrothermal alteration and evolution of the Ohakuri hydrothermal system, Taupo volcanic zone, New Zealand. J. Volcanol. Geoth. Res. 34 (3–4), 211–231. https://doi.org/10.1016/0377-0273(88)90034-0.

Howard, D.L., de Jonge, M.D., Afshar, N., Ryan, C.G., Kirkham, R., Reinhardt, J., Kewish, C.M., McKinlay, J., Walsh, A., Divitcos, J., Basten, N., Adamson, L., Fiala, T., Sammut, L., Paterson, D.J., 2020. The XFM beamline at the Australian Synchrotron. J. Synchrotron Radiat. 27, 1447–1458.

Jones, B., Renaut, R.W., 2003. Hot spring and geyser sinters: the integrated product of precipitation, replacement, and deposition. Can. J. Earth Sci. 40, 1549–1569.

Krupp, R.E., Seward, T.M., 1987. The Rotokawa geothermal system, New Zealand; an active epithermal gold-depositing environment. Econ. Geol. 82 (5), 1109–1129.

Li, F., Liu, F., Huang, K., Yang, S., 2022a. Advancement of gallium and gallium-based compounds as antimicrobial agents. Front. Bioeng. Biotechnol. 10, 827960. https://doi.org/10.3389/fbioe.2022.827960.

Li, Y., Fu, S., Zhang, Q., Liu, H., Wang, Y., 2022b. Recent Progress of Ga-based catalysts for catalytic conversion of light alkanes. Catalysts 12, 1371. https://doi.org/10.3390/catal12111371.

Lo, Y.-C., Cheng, C.-L., Han, Y.-L., Chen, B.-Y., Chang, J.-S., 2014. Recovery of high-value metals from geothermal sites by biosorption and bioaccumulation. Bioresour. Technol. 160, 182–190.

Lu, F., Xiao, T., Lin, J., Ning, Z., Long, Q., Xiao, L., Huang, F., Wang, W., Xiao, Q., Lan, X., Chen, H., 2017. Resources and extraction of gallium: a review. Hydrometallurgy 174, 105–115.

Lynne, B.Y., 2012. Mapping vent to distal-apron hot spring paleo-flow pathways using siliceous sinter architecture. Geothermics 43, 3–24. https://doi.org/10.1016/j.geothermics.2012.01.004.

Lynne, B.Y., Campbell, K.A., James, B.J., Browne, P.R.L., Moore, J., 2007. Tracking crystallinity in siliceous hot-spring deposits. Am. J. Sci. 307, 612–641.

Lynne, B.Y., Campbell, K.A., Moore, J.N., Browne, P.R.L., 2005. Diagenesis of 1900-year-old siliceous sinter (opal-A to quartz at Opal Mound, Roosevelt Hot Springs, Utah, U.S.A. Sediment. Geol. 179, 249–278.

Lynne, B.Y., Campbell, K.A., 2003. Diagenetic transformations (opal-A to quartz) of low- and mid-temperature microbial textures in siliceous hot-spring deposits, Taupo Volcanic Zone, New Zealand. Can. J. Earth Sci. 40 (11), 1679–1696.

Lynne, B.Y., Campbell, K.A., 2006. Diagenesis and Dissolution at Sinter Island (456 Yrs BP), Taupo Volcanic Zone: Silica Stars and the Birth of Quartz. 28th NZ Geothermal Workshop.

Lyon, B.J., Rowe, M.C., Langendam, A., Campbell, K.A., Guido, D.M., Hamilton, A.R., Nersezova, E.E., Galar, A., Stallard, D.A., 2026. Impact of diagenesis and acidic alteration on microbial fabrics and trace element distributions in fossilised siliceous hot spring deposits. Geochimica et Cosmchimica Acta. https://doi.org/10.1016/j.gca.2026.02.022.

Makishima, A., Tanaka, R., Nakamura, E., 2009. Precise elemental and isotopic analyses in silica samples employing ICP-MS: applications of hydrofluoric acid solution and analytical techniques. Anal. Sci. 25 (10), 1181–1187.

Makishima, A., Nakamura, E., 2006. Determination of major/minor and trace elements in silicate samples by ICP-QMS and ICP-SFMS applying isotope dilution-internal standardisation (ID-IS) and multi-stage internal standardisation. Geostand. Geoanal. Res. 30 (3), 245–271.

Mare, E.R., O'Neill, H.StC., Berry, A.J., Frigo, C., Glover, C.J., 2021. Coordination change of Ge4+ and Ga3+ in silicate melt with pressure. Geochem. Cosmochim. Acta 303, 184–204.

Minandri, F., Bonchi, C., Frangipani, E., Imperi, F., Visca, P., 2014. Promises and failures of gallium as an antibacterial agent. Future Microbiol. 9 (3), 379–397.

Morris, R.E., Brammer, L., 2017. Coordination change, lability and hemilability in metal-organic frameworks. Chem. Soc. Rev. 46, 5444–5462.

Moskalyk, R.R., 2003. Gallium: the backbone of the electronics industry. Miner. Eng. 16 (10), 921–929.

Nakamura, E., Kobayashi, K., Tanaka, R., Kunihiro, T., Kitagawa, H., Potiszil, C., et al., 2022. On the origin and evolution of the asteroid Ryugu: a comprehensive geochemical perspective. In: Proceedings of the Japan Academy, Series B, 98, pp. 227–282.

Nakamura, E., Makishima, A., Moriguti, T., Kobayashi, K., Sakaguchi, E., Yokoyama, T., et al., 2003. Comprehensive geochemical analyses of small amounts (∼100 mg) of extraterrestrial samples for the analytical competition related to sample return mission MUSES-C. Inst. Space Astronautical Sci. Rep. 16, 49–101.

Nersezova, E.E., Rowe, M.C., Campbell, K.A., Langendam, A., Tollemache, C., Lyon, B., Galar, A., Guido, D.M., Teece, B.L., Hamilton, T.L., 2024. Trace metal and organic biosignatures in digitate stromatolites from terrestrial siliceous hot spring deposits: implications for the exploration of martian life. Chem. Geol. 661. https://doi.org/10.1016/j.chemgeo.2024.122194.

Nersezova, Ema E., Rowe, Michael C., Campbell, Kathleen A., Ang, Andrew, Matthews, Steve, Ruff, Steven W., Meghwal, Ashok, Adam, Ludmila, Galligan, Niamh, Loho, Thomas, 2023. Exploring the internal textures and physical properties of digitate sinter in hot springs: Implications for remote sampling on Mars. Planetary and Space Science 238, 105786. https://doi.org/10.1016/j.pss.2023.105786, 105786. https://linkinghub.elsevier.com/retrieve/pii/S0032063323001551.

Nishi, K., Shimizu, K.I., Takamatsu, M., Yoshida, H., Satsuma, A., Tanaka, T., Yoshida, S., Hattori, T., 1998. Deconvolution analysis of Ga K-Edge XANES for quantification of gallium coordinations in oxide environments. The Journal of Physical Chemistry B 102 (50), 10190–10195.

Parry, W.T., Nash, W.P., Bowman, J.R., Ward, S.H., Whelan, J.A., Bryant, N.L., Deodolph, R.E., Evans Jr, S.H., Bowers, D., 1977. Geology and geochemistry of the Roosevelt Hot Springs thermal area. Utah—A summary: salt Lake City, University of Utah Department of geology and Geophysics, Final Report. DOE/DGE Contract EY-76-S-07-1601 (part 1) 1–12.

Pokrovski, G.S., Schott, J., Hazemann, J.-L., Farges, F., Pokrovsky, O.S., 2002. An X-ray absorption fine structure and nuclear magnetic resonance spectroscopy study of gallium-silica complexes in aqueous solution. Geochem. Cosmochim. Acta 66 (24), 4203–4322.

Pokrovsky, O.S., Pokrovski, G.S., Schott, J., 2004. Gallium(III) adsorption on carbonates and oxides: X-ray absorption fine structure spectroscopy study and surface complexation modelling. J. Colloid Interface Sci. 279, 314–325.

Pope, J.G., Brown, K.L., McConchie, D.M., 2005. Gold concentrations in springs at Waiotapu, New Zealand: implications for precious metal deposition in geothermal systems. Econ. Geol. 100, 677–687.

Qi, H., Gong, N., Zhang, S.-Q., Li, J., Yuan, G.-L., Liu, X.-F., 2023. Research progress on the enrichment of gallium in bauxite. Ore Geol. Rev. 160, 105609. https://doi.org/10.1016/j.oregeorev.2023.105609.

Qin, S., Sun, Y., Li, Y., Wang, J., Zhao, C., Gao, K., 2015. Coal deposits as promising alternative sources for gallium. Earth Sci. Rev. 150, 95–101.

Ravel, B., Newville, M., 2005. ATHENA, ARTEMIS, HEPHAESTUS: data analysis for X-ray absorption spectroscopy using IFEFFIT. J. Synchrotron Radiat. 12, 537–541.

Rice, C.M., Ashcroft, W.A., Batten, D.J., Boyce, A.J., Caulfield, J.B.D., Fallick, A.E., Hole, M.J., Jones, E., Pearson, M.J., Rodgers, G., Saxton, J.M., Stuart, F.M., Trewin, N.H., Turner, G., 1995. A Devonian auriferous hot spring system, Rhynie, Scotland. J. Geol. Soc. London 152, 229–250.

Rowe, M.C., Campbell, K.A., Hamilton, A., Jiang, Y., Pelser, J., Murphy, B., Martin, R., Mackenzie, K.M., Stallard, D.A., Lyon, B., Langendam, A., Nersezova, E.E., Guido, D.M., Rowland, J.V., 2025. Life and death of a sinter archive: evolution of siliceous hot-spring deposits (Holocene) on the dynamic Paeroa fault at Te Kopia, Taupo Volcanic Zone, New Zealand. J. Volcanol. Geoth. Res. 465. https://doi.org/10.1016/j.jvolgeores.2025.108380.

Rudnick, R.L., Gao, S., 2003. Composition of the continental crust. In: Treatise on geochemistry, 3, pp. 1–64.

Ryan, C.G., Cousens, D.R., Sie, S.H., Griffin, W.L., Suter, G.F., Clayton, E., 1990. Quantitative pixe microanalysis of geological material using the CSIRO proton microprobe. Nucl. Instrum. Methods Phys. Res., Sect. A B (47), 55–71.

Ryan, C.G., Kirkham, R., Hough, R.M., Moorhead, G., Siddons, D.P., de Jonge, M.D., Paterson, D.J., De Geronimo, G., Howard, D.L., Cleverly, J.S., 2010. Elemental X-ray imaging using the Maia detector array: the benefits and challenges of large solid angle. Nucl. Instrum. Methods Phys. Res., Sect. A 619 (1–3), 37–43.

Ryan, C.G., Laird, J.S., Fisher, L.A., Kirkham, R., Moorhead, G.F., 2015. Improved dynamic analysis method for quantitative PIXE and SXRF element imaging of complex materials. Nucl. Instrum. Methods Phys. Res., Sect. B 363, 42–47.

Sanchez-Yanez, C., Reich, M., Leisen, M., Morata, D., Barra, F., 2017. Geochemistry of metals and metalloids in siliceous sinter deposits: implications for elemental partitioning into silica phases. Appl. Geochem. 80, 112–133.

Sriaporn, C., Campbell, K.A., Millan, M., Ruff, S.W., Van Kranendonk, M.J., Handley, K. M., 2020. Stromatolitic digitate sinters from under wide-ranging physicochemical conditions with diverse hot spring microbial communities. Geobiology 18 (5), 619–640. https://doi.org/10.1111/gbi.12395.

Walter, M.R., Desmarais, D., Farmer, J.D., Hinman, N.W., 1996. Lithofacies and biofacies of mid-paleozoic thermal spring deposits in the Drummond Basin, Queensland, Australia. Palaios 11 (6), 497–518.

Walter, M.R., Grotzinger, J.P., Schopf, J.W., 1992. Proterozoic stromatolites. In: Schopf, J.W., Klein, C. (Eds.), Proterozoic Biosphere, a multi-disciplinary Study. Cambridge University Press, pp. 253–260.

Watts-Henwood, Nick, Campbell, Kathleen A., Lynne, Bridget Y., Guido, Diego M., Rowland, Julie V., Browne, Patrick R.L., 2017. Snapshot of hot-spring sinter at Geyser Valley, Wairakei, New Zealand, following anthropogenic drawdown of the geothermal reservoir. Geothermics 68, 94–114. https://doi.org/10.1016/j.geothermics.2017.03.002. https://linkinghub.elsevier.com/retrieve/pii/S0375650516302024.

Weissberg, B.G., 1969. Gold-silver ore-grade precipitates from New Zealand thermal waters. Econ. Geol. 64, 95–108.

Wood, S.A., Samson, I.M., 2006. The aqueous geochemistry of gallium, germanium, indium, and scandium. Ore Geol. Rev. 28, 57–102.

Yokoyama, T., Makishima, A., Nakamura, E., 1999. Evaluation of the coprecipitation of incompatible trace elements with fluoride during silicate rock dissolution by acid digestions. Chem. Geol. 157 (3–4), 175–187. https://doi.org/10.1016/S0009-2542(98)00206-X.

Yuan, W., Chen, J., Teng, H., Chetelat, B., Cai, H., Liu, J., Wang, Z., Bouchez, J., Moynier, F., Gaillardet, J., Schott, J., Liu, C., 2021. A review on the elemental and isotopic geochemistry of gallium. Glob. Biogeochem. Cycles 35. https://doi.org/10.1029/2021GB007033.

Zhao, Z., Yang, Y., Xiao, Y., Fan, Y., 2012. Recovery of gallium from Bayer liquor: a review. Hydrometallurgy 125–126, 115–124.